

Velocity measurements of a shear flow penetrating a porous medium

By MARK F. TACHIE†, DAVID F. JAMES
AND IAIN G. CURRIE

Department of Mechanical and Industrial Engineering, University of Toronto, Toronto,
Canada, M5S 3G8

(Received 5 December 2002 and in revised form 14 May 2003)

This paper reports an experimental investigation of simple shear flow penetrating a model of a fibrous porous medium. The flow field is established between a stationary inner cylinder and a concentric outer cylinder rotating at a constant speed. The model medium is a regular array of rods which are oriented across the flow and which fill a fraction of the annular space between the cylinders. Rods with circular, square and triangular cross-sections are investigated, and the solid volume fraction of the arrays ranges from 0.01 to 0.16. With a viscous oil as the working fluid, the Reynolds number is much less than unity. Velocity measurements made using particle image velocimetry focus on the region around the edge of each array tested. The measurements reveal that eddies form between the two outermost circles of rods, for solid volume fractions above a minimum value which depends on rod shape. The velocity data are used to find the interfacial slip velocity and the average velocity at the interface between the porous medium and the outer shear flow. The data demonstrate that the slip velocity decays with increasing solid volume fraction, as expected, but the velocity is found to be nearly independent of rod shape and of the number of circles of rods comprising an array. It is also found that the slip velocity is only 24–30% of the value predicted from the Brinkman equation.

1. Introduction

Darcy's law generally governs flow within a porous medium, but not near an edge of the medium. When the edge is adjacent to a solid boundary, for example, there is a shear component in the bulk velocity and the law is not applicable when the flow contains a rotational component. Similarly, when the edge is adjacent to a channel so that it forms the boundary of the channel, then the flow parallel to the edge extends into the medium, especially when the medium is highly porous. In this case, the bulk velocity increases from its interior Darcy value as the edge is approached, creating a boundary layer flow with the medium along its edge. The simplest case of flow penetration is simple shear flow outside the medium with no pressure gradient, so that the interior velocity is zero. In this case, the boundary-layer flow generates a 'slip velocity' at the interface between the medium and the external flow, and this velocity is the boundary condition for both the internal and external flows. For a compact porous medium, the slip velocity is virtually zero and the no-slip boundary condition

† Present address: Department of Mechanical and Industrial Engineering, University of Manitoba, Canada, R3T 5V6.

is a safe assumption in almost every case. However, when the medium is highly permeable, the no-slip condition may not be appropriate. The highly porous media which give rise to this situation are necessarily media consisting of long particles or fibres. Insulation and filters are examples of such media, as are polymer brushes. This type of brush is formed when polymer chains in solution attach themselves to an immersed surface. The randomly coiled chains extend out from the surface, producing a porous layer adjacent to the surface. Polymer brushes are found in dispersions when colloidal particles are coated with polymer, and brushes are formed in fine pores when a polymer solution flows through the pores and some of the chains adsorb to the surface. In these cases, fluid flows through the porous brush as well as over it and we generally want to know the degree of penetration of the outer flow, or the slip velocity at the surface. Knowledge of the latter is necessary for the calculation of flow rates inside and outside the porous medium. Penetration is also of interest because it is related to diffusion, i.e. to the rates of heat and mass transfer between the external and internal flows.

Of the little information in the literature about penetration and slip velocity, most is theoretical, although the first study was experimental (Beavers & Joseph 1967). They determined the boundary condition by flow rate measurements in a channel bounded on one side by a porous medium, and they presented results for several natural and manufactured porous media in terms of a dimensionless slip coefficient α , the values of which were found to be of order unity. In the present work, results will be given in terms of a dimensionless slip velocity, $U_s/\sqrt{k}\dot{\gamma}$, where U_s is the slip velocity, k is the permeability of the medium and $\dot{\gamma}$ is the shear rate at the interface. This group – introduced in James & Davis (2001 hereinafter referred to as J&D) – is the inverse of α and is preferred here because slip velocity is the quantity of primary interest. The results from Beavers & Joseph, in terms of this latter group, range from 0.25 to about 10. These values may be put in context by comparing them to the value predicted by the Brinkman equation (Brinkman 1947), which is used to estimate the slip velocity. By matching the solution of Stokes equation for the external flow to the solution of Brinkman's equation for the porous medium flow, it is found that $U_s/\sqrt{k}\dot{\gamma}$ is equal to 1.0 (J&D). As such, it lies in the middle of the experimental values. Apart from the data to be reported in this paper, the results from Beavers & Joseph and Taylor (1971) appear to be the only experimental values available.

More studies have been carried out by theoretical methods. One of the best known theoretical works is that by Richardson (1971) who solved Stokes equation for flow over and through deep rectangular grooves in a plate. He found that $U_s/\sqrt{k}\dot{\gamma}$ depends on the ratio of the groove thickness to the wall thickness, and that its maximum value is 0.7 for this geometry. Larson & Higdon (1986, 1987) used numerical methods to solve Stokes equation for simple shear flow over a square array of rods aligned with the flow (1986) and across the flow (1987). They used two methods to find the slip velocity, one based on the flow rate above the slip plane and the other on the rate below. The two techniques yielded different results, generally different by an order of magnitude and sometimes different even in sign. Their work, then, does not yield useful information about the slip velocity. For the arrays across the flow, they reported that eddies form within the porous media at higher solid volume fractions. Another numerical investigation, by Sahraoui & Kaviany (1991), also dealt with flow across arrays of rods. They obtained values for the slip coefficient, but their results pertain to barely permeable media and thus have limited usefulness. To explain this remark further, the slip velocity is significant only when the solid volume fraction of the medium is below 0.1 (which will be demonstrated shortly by a numerical

example). In Sahraoui & Kaviany, the solid volume fraction was a minimum of 0.2 and generally around 0.5. Hence, the slip velocities they found are extremely small and have virtually no effect on flow in the adjacent channel.

The same Stokes flow problem of shear flow across an array of rods was tackled by analytical methods (J&D). To create the physical situation, a square array of rods was installed next to one wall in a planar channel, partially filling the channel, and the other wall was moved at a constant speed. This motion generated shear flow across the rods and simple shear flow in the space between the rods and the moving wall. The small parameter in their analysis was the solid volume fraction ϕ , the fraction of the volume occupied by the rods, and the accuracy of their calculations was to order ϕ because terms of order ϕ^2 were neglected in satisfying the no-slip condition at the surface of the rods. They defined the slip plane – the interface between the outer flow and the porous medium – as the plane tangent to the edges of the outermost rods, and calculated the average velocity on that plane. Their results show that the dimensionless slip velocity $U_s/\sqrt{k}\dot{\gamma}$ depends only on ϕ , and not on other geometrical parameters such as the number of rows in the array, or on the fraction of the channel width occupied by the array. Furthermore, $U_s/\sqrt{k}\dot{\gamma}$ was found to depend only weakly on ϕ . For example, as ϕ increases from 0.001 to 0.1, $U_s/\sqrt{k}\dot{\gamma}$ decreases from 0.29 to 0.23. Hence, the slip velocity U_s increases approximately as \sqrt{k} , or as the length scale of the porous medium. For a square array of rods of radius a , k is given by (e.g. Jackson & James 1986)

$$\frac{k}{a^2} = \frac{1}{8\phi} \left[\ln \frac{1}{\phi} - 1.476 + 2\phi + O(\phi^2) \right]. \quad (1)$$

When the distance between rods is L , $\phi = \pi a^2/L^2$, the equation shows that \sqrt{k} is roughly proportional to L for widely separated rods and is specifically $0.35L$ for ϕ equal to 0.01. Hence, the work of J&D predicts that the slip velocity U_s increases approximately linearly with L , which is physically reasonable.

The dimensionless representation of the slip velocity does not indicate just how large or small U_s is, and an illustration may help. Suppose that the solid volume fraction ϕ of a square array is 0.1 and that the array fills half the width D of a channel. If the speed of the moving wall is U , then the approximate shear rate $\dot{\gamma}$ in the channel and at the interface is $2U/D$. If there are five rows in the array, L/D is $1/10$, and the shear rate is $20U/L$. According to (1), \sqrt{k} is about $0.20L$, and, since $U_s/\sqrt{k}\dot{\gamma}$ is about 0.25 (J&D), U_s/U is then 0.010. This example demonstrates that the slip velocity is a small fraction of the velocity in the outer flow, even when the rods occupy only 10% of the total area. For most practical purposes, the slip velocity in this case can be taken to be zero. This example also confirms the statement made above that the slip velocity is generally significant only when ϕ is below 0.1. It also justifies the use of analytical methods in which ϕ is the small parameter.

One other point should be made about the dimensionless slip velocity value of 0.25: this value is much less than the value of 1.0 derived from the Brinkman equation. The Brinkman equation has been used for some time because no other information has been available, but its usefulness is now demonstrated to be limited, at least for flow across an array of rods.

The calculations of $U_s/\sqrt{k}\dot{\gamma}$ by J&D were carried out for ϕ from 0.0001 to 0.1, but the accuracy of their results is not known when ϕ is of order 0.1 because of neglected ϕ^2 terms. Since filters and other fibrous materials have ϕ values in this range, reliable values of $U_s/\sqrt{k}\dot{\gamma}$ are desirable when ϕ is $O(0.1)$, the range not covered by the

theory. Hence, we initiated an experimental programme to assess the theory for ϕ less than 0.1 and to make measurements for ϕ above 0.1 in order to have results for all practically important solid volume fractions. The theoretical work in J&D was rectilinear, but circular motion was chosen for the experimental work because generating a shear flow next to a porous medium is much easier in a circular geometry than in a rectilinear one. The radius of curvature of the circular flow was made large enough that curvature could be ignored, making it possible to plot experimental and theoretical results together. The circular motion was created by having a viscous liquid fill the annular space between two concentric drums, the inner one being stationary and the outer one rotating at a constant speed, with a stationary array of rods filling a portion of the annulus next to the inner wall. Descriptions of the experimental set-up and technique are given in Shams (2000) and Shams, James & Currie (2003). The initial concern of the experimental programme was secondary motion because Larson & Higdon (1987) predicted by numerical methods that such motion occurs in a square array, generally between the first two rows, in the ϕ range of 0.03 to 0.1. In this range, the rods are widely spaced and so eddies are unexpected, particularly in a shear-driven flow. Hence, Shams *et al.* set out to examine the flow patterns within an array using particle image velocimetry (PIV). Flow patterns were recorded for arrays of circular rods for three solid volume fractions between 0.025 and 0.1. Eddies were indeed found, although not exactly in the locations predicted by Larson & Higdon.

Subsequent work then focused on velocity measurements covering a wider range of solid volume fraction and employing non-circular rods as well as circular ones. Arrays were constructed with ϕ between 0.01 and 0.16. The lower part of this range overlaps with the accurate range of J&D and the higher part extends to practical values. Non-circular shapes cannot be explored easily by analytical methods, and so arrays were made with non-circular rods to study the influence of shape.

There was a second objective. In J&D, it was found that the outer flow penetrates the array only a short distance – a fraction of the distance to the second row – independently of the value of ϕ . Hence, interior rods in an array apparently have only a minor role in bringing the flow to rest there. In a subsequent theoretical study, this possibility was explored by calculating the slip velocity as interior rows of rods were sequentially removed, starting in the interior and eventually leaving only the outermost row for the final calculation (Davis & James 2003). It was found that the interior rows indeed had little influence because the slip velocity for the last row was virtually the same as that for a full array. We wanted to verify this surprising result experimentally, and so the present work included velocity measurements with single rows of rods.

2. Experimental design and measurement procedure

2.1. Design considerations for the channel

As indicated above, the basic flow investigated in this work is flow between circular cylinders with a fraction of the annulus filled with regular arrays of rods. The experimental set-up is shown in figure 1. The rods and inner cylinder are stationary and, with the outer cylinder rotating at a constant speed, circular Couette flow is generated between the outermost rods and the outer rotating cylinder. To facilitate optical access to the flow field and to minimize optical distortion, the cylinders were made of 6 mm thick transparent acrylic and the rods were transparent as well. The outer cylinder was fixed to an acrylic disk to create an open tank which was mounted on a variable-speed direct-drive turntable. The inner cylinder was fixed to a stationary

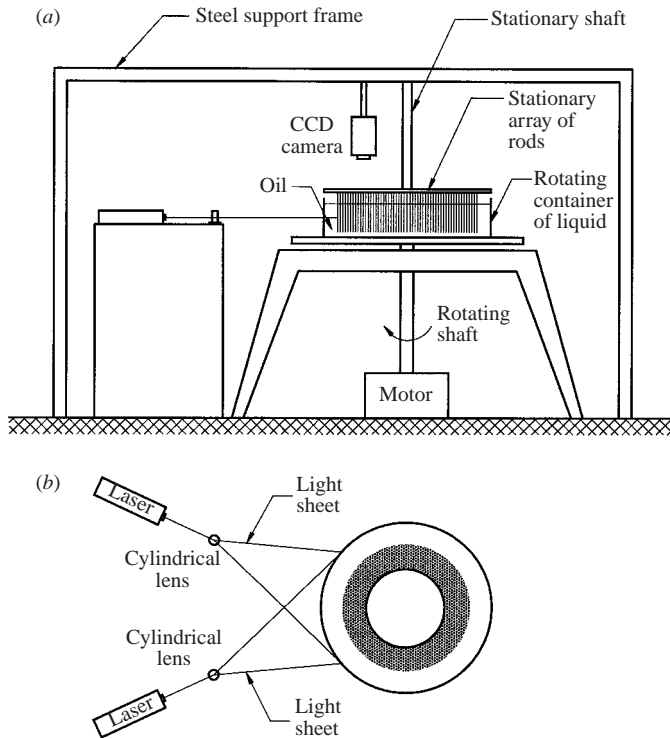


FIGURE 1. The experimental set-up, shown (a) in side view and (b) in plan view. A rod array was hung upside down in a drum of oil rotating on a turntable. Two lasers created a sheet of light in a horizontal plane below the free surface of oil, illuminating seeding particles for determining the velocity field by PIV.

transparent acrylic disk supported from above by a steel frame. The outer radius R_i of the inner cylinder was approximately 140 mm, and the inner radius R_o of the outer cylinder was 222 mm. The height H of the open tank was 125 mm, and the depth of the working fluid was approximately 120 mm.

2.2. Design of the model porous media

Each model porous medium consisted of a regular array of rods inserted into holes drilled into an acrylic disk. The holes were drilled on circles and rays and spaced to form a quasi-square array (because of the large radii of curvature). As shown in figure 1, the disk was suspended above the tank with the rods facing downwards. The length of the rods below the free surface was approximately 110 mm so that the clearance between the bottom of the rods and the base of the tank was approximately 10 mm. A schematic top view of the cylinders is shown in figure 2. For clarity, only some of three circles of rods are shown. The figure also defines the Cartesian coordinates used to identify positions in the flow field where PIV measurements were made: x denotes the streamwise direction, y denotes the transverse direction, positive away from the array. Cartesian coordinates were used because they were more practical than circular coordinates for the large radii of curvature.

In the present work, three different shapes of rod were studied: circular, square and triangular. The spacing L of rods between and along circles was chosen to achieve a constant solid volume fraction ϕ . For a quasi-square array of rods, the cross-sectional

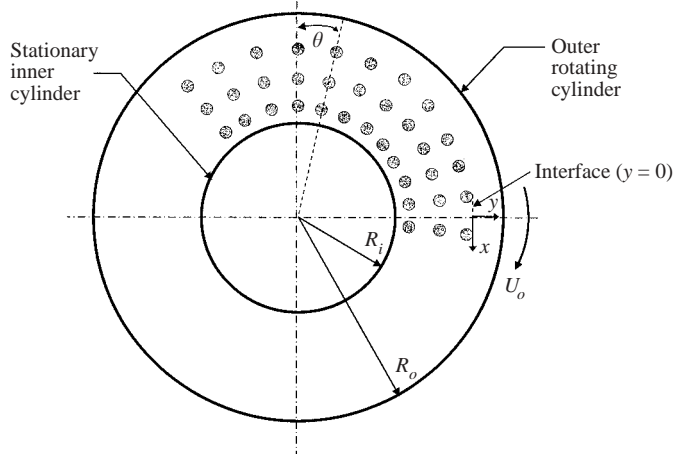


FIGURE 2. Top view of the experimental arrangement showing the stationary inner cylinder of radius R_i , the outer cylinder of radius R_o rotating at constant speed U_o and some of 3 circles of circular rods. The plain medium-porous medium interface is defined as the tangent to the outer edges of rods in the outermost circle; x denotes the streamwise direction and y denotes the transverse direction, positive away from the array.

area of the rods A , the rod spacing L and the solid volume fraction ϕ are related by

$$\phi = \frac{A}{L^2}. \quad (2)$$

As the equation indicates, the solid volume fraction can be varied by changing the size of rods or the spacing between them. One consideration was that, since the velocity measurements would be made using PIV, L should be sufficiently small to achieve high spatial resolution. At the same time, the rods had to be large enough to resist bending caused by the flow. For circular rods, these demands were satisfied by a diameter of 3.18 mm, following an exploratory investigation by Shams (2000). Similarly, the square rods had a side length of 3.18 mm and the rods with an equilateral triangular cross-section had a side length of 6.36 mm.

In all of the arrays, the radius of the outermost circle of rods was $R_1 = 198.4$ mm so that R_1/R_o was about 0.9. Thus, the gap between the outermost circle of rods and the outer rotating cylinder was approximately 24 mm. The results presented later will show that this gap was sufficient to establish a Couette velocity distribution between the outermost circle of rods and the rotating cylinder. Given R_1 and the rod size, two different approaches were used to obtain quasi-square arrays with uniform solid volume fractions. In the first approach, the holes were drilled at the intersections of rays and circles. The following calculations illustrate how circle radii were determined. For the case for $\phi = 0.16$, the spacing of rods of radius a on the outermost circle is, according to (2),

$$L_1 = a \sqrt{\frac{\pi}{\phi}} = 1.59 \sqrt{\frac{\pi}{0.16}} = 7.09 \text{ mm}. \quad (3)$$

The angular spacing between rods on this circle is

$$\theta = \frac{L_1}{R_1} = 0.03574 \text{ rad}. \quad (4)$$

	ϕ	L_1 (mm)	R_1 (mm)	R_2 (mm)	R_3 (mm)	R_4 (mm)	R_5 (mm)	M	N
(a)	0.01	28.2	198.4	167.9	NA	NA	NA	2	44
	0.025	17.8	198.4	179.7	158.9	NA	NA	3	70
	0.04	14.1	198.4	183.8	167.9	NA	NA	3	88
	0.052*	12.4	198.4	186.0	173.6	161.3	148.9	5	NA
	0.10	8.9	198.4	189.3	179.7	169.6	158.9	5	140
	0.16	7.0	198.4	191.2	183.8	176.0	167.9	5	177
	ϕ	L_1 (mm)	R_1 (mm)	R_2 (mm)	N				
(b)	0.025	20.1	198.4	178.3	62				
	0.04	15.9	198.4	182.5	79				
	0.05	14.2	198.4	184.2	88				
	0.10	10.1	198.4	188.3	124				
	0.16	8.0	198.4	190.5	157				
(c)	0.025	28.5	198.4	169.9	44				
	0.04	22.5	198.4	175.9	56				
	0.05	20.1	198.4	178.3	62				
	0.10	14.2	198.4	184.2	88				
	0.16	11.3	198.4	187.2	111				

TABLE 1. Summary of geometrical parameters for the three different shapes of rods investigated; L_1 is the spacing between adjacent rods in the outermost circle, R_1 is the radius of the outermost circle of rods, R_2 is the radius of the second circle of rods etc, M is the number of rows for a full array of rods, N is the number of rods per circle. (a) Circular rods with $d = 3.18$ mm; $44 \leq N \leq 177$; $2 \leq M \leq 5$. (b) Square rods with 3.18×3.18 mm² cross-section, $62 \leq N \leq 157$, $M = 3$. (c) Triangular rods with each side being 6.36 mm, $44 \leq N \leq 111$, $M = 2$.

For this value of θ , the radii of successive circles are obtained from

$$R_{n+1}^2 - R_n^2 = \frac{2A}{\theta\phi}. \quad (5)$$

From this equation, the radius of the second circle R_2 was found to be 191.2 mm. The values of L and R for the other circles were calculated using (4) and (5), and the number of rods on each circle was determined from:

$$N = \frac{2\pi R_1}{L_1} = 176. \quad (6)$$

By the present approach, N is constant for a given value of ϕ , and the distance between successive radii increases slightly inward. This calculation method was used to design all of the arrays (i.e. circular, square and triangular) except for the array with circular rods at $\phi = 0.052$. For this array, uniform spacing was maintained in both the radial and circumferential directions. Consequently, four rods in the edge region only formed a square at one location, and it was at that location that PIV measurements were made.

The important geometrical parameters for the arrays of circular, square and triangular rods are given in table 1, where M is the number of circles of rods and N is the number of rods per circle. The table indicates that the minimum number of rods per circle is 44. Although this may seem too few to ignore curvature effects, an analysis by Davis & James (2003) reveals that 16 rods per circle is sufficient for curvature to be neglected. One of our objectives was to explore the flow field with a single circle of rods, i.e. with $M = 1$, and thus 'arrays' were made with a single circle

of rods, some with circular rods and the others with square rods. The first arrays were made with five circles ($M = 5$), but subsequent work showed that the details of the flow field in the interfacial region are nearly independent of the number of circles provided that M is at least two. Hence, later arrays were made with two or three circles of rods ($M \geq 2$) and these will be referred to as full arrays. The arrays with one circle will be referred to as single arrays.

2.3. Experimental arrangement and measurement procedure

The experiments were conducted in the vertical circular Couette apparatus described earlier. Silicon oil (GE Silicone), having a kinematic viscosity ν of $1000 \text{ mm}^2 \text{ s}^{-1}$ at room temperature, was used as the working fluid. The velocity of the outer rotating cylinder U_o varied from 19 to about 26 mm s^{-1} . Hence the Reynolds number, based on U_o and rod size, was approximately 0.07 for the circular and square rods and 0.15 for the triangular rods. Both the oil and the acrylic plastic were transparent, and because their refractive indices are similar, it was possible for a laser sheet to pass through the fluid as well as the acrylic cylinder and rods without appreciable distortion. The flow was seeded with silver-coated spherical hollow glass beads, having a mean diameter of $14 \mu\text{m}$ and a specific gravity of 1.65. From these values, the settling velocity of the particles is estimated to be $7.5 \times 10^{-5} \text{ mm s}^{-1}$, which means that the particles were virtually stationary during the few minutes it took to complete a run. The particle response time was estimated to be $1.9 \times 10^{-8} \text{ s}$, which ensured that the particles faithfully followed the flow. The particle concentration was such that there were between 12 and 20 of them in each PIV interrogation region.

The test section was primarily illuminated by a 50 mW argon ion laser ($\lambda = 532 \text{ nm}$). A second laser (20 mW and $\lambda = 532 \text{ nm}$) was positioned at about 20° to the 50 mW laser to improve illumination within the array. Each laser beam was transformed into a light sheet approximately 1 mm thick using a 20 mm cylindrical glass rod having a focal length of 555 mm. Each sheet was horizontal and located approximately 80 mm above the tank bottom, or about 40 mm below the free surface. At this location, the flow was approximately two-dimensional and free surface effects were negligible. Secondary flow was possible in the open region of the annular channel, but observations with the PIV system verified there was no such motion. The other region of concern was under the rods because the rotation of the nearby tank bottom made the flow there three-dimensional. Exploratory measurements by Shams (2000) revealed secondary motion in that region, extending upward a distance of about half the rod spacing. This extent was found to be independent of the gap between the rod tips and the bottom of the tank. To ensure that this motion did not affect the flow in the rest of the array, it was eliminated by attaching an annular disk to the bottom of the array covering the tips.

The velocity measurements were made within a unit cell, i.e. the nearly square space formed by four rods at the edge of an array plus a small region outside in the main flow. The camera was a Progressive Scan Pulnix TM-9701, an analogue monochrome charged-coupled device (CCD) with 768×484 square-pixel chips. The camera operated at 30 frames per second and was fitted with a C-mount lens. Images from it were converted digitally and stored continuously at 30 Hz in a computer using a DT 3152 frame grabber board (Data Translation). To minimize the lengths of particle streaks, electronic shutter speeds were between $1/500$ and $1/2000 \text{ s}$. The digital images were post-processed using a commercial fast Fourier transform based cross-correlation scheme (VISIFLOW, AEA Technology). The 768×484 pixel image

Test	Shape of rod	Solid volume fraction ϕ	Number of rows M	Array qualification	Velocity U_o (mm s ⁻¹)
1	Circular	0.01	2	Full	20.12
2	Circular	0.025	3	Full	21.33
3	Circular	0.04	3	Full	23.04
4	Circular	0.052	5	Full	25.14
5	Circular	0.10	5	Full	19.36
6	Circular	0.16	5	Full	20.33
7	Circular	0.01	1	Single	20.82
8	Circular	0.025	1	Single	24.91
9	Circular	0.04	1	Single	21.46
10	Circular	0.052	1	Single	20.82
11	Circular	0.10	1	Single	24.91
12	Circular	0.16	1	Single	22.52
13	Square	0.025	2	Full	22.14
14	Square	0.04	2	Full	24.47
15	Square	0.05	2	Full	22.50
16	Square	0.10	2	Full	21.46
17	Square	0.16	2	Full	25.36
18	Square	0.025	1	Single	23.25
19	Square	0.04	1	Single	24.91
20	Square	0.05	1	Single	20.82
21	Square	0.10	1	Single	22.50
22	Square	0.16	1	Single	22.87
23	Triangular	0.025	2	Full	19.11
24	Triangular	0.04	2	Full	19.92
25	Triangular	0.05	2	Full	20.93
26	Triangular	0.10	2	Full	20.82
27	Triangular	0.16	2	Full	21.80

TABLE 2. Summary of test conditions, U_o is the velocity of the outer rotating cylinder.

plane of the camera was divided into 64×64 pixel subregions with 75% overlap to give a typical spatial resolution of 0.8 mm.

Velocities inside the arrays were found to be one to four orders of magnitude lower than those in the exterior flow. Because of this wide range, it was necessary to divide the flow field into subregions, and then different combinations of images from those subregions were used to obtain the velocity vectors. In the outer flow where the velocity was high, adjacent images were processed with the minimum time interval of 1/30 s. Within an array, where the velocity was tiny by comparison, several frames were skipped between successively acquired images. In this region, time intervals between 0.5 and 2.5 s were used to obtain the velocity vectors. Mean velocities were obtained using 30 or more images for each value.

Velocity measurements were made for 27 cases altogether, covering three rod shapes (circular, square and triangular) and various solid volume fractions ($0.01 \leq \phi \leq 0.16$), and single versus full arrays. The test conditions for the 27 cases are given in table 2.

2.4. Uncertainty analysis

An uncertainty analysis was made following the procedure outlined in the AIAA Standard (Coleman & Steele 1995). The total uncertainty is composed of a bias component (B) and a precision component (P). The primary sources of bias uncertainty in PIV measurements are particle inability to follow the flow, timing precision, and errors arising from the peak-finding algorithm to determine average

particle displacement. A particle's ability to follow the flow is related to its response time. Since the response time is extremely small (2×10^{-8} s) and since the particle density is close to the fluid density, the particles are considered to follow the fluid accurately. As to timing error, the CCD has a minimum frame period of 33.3 ms and a frame transfer rate of 0.5 ms. Thus the timing error is estimated to be 1.5%. The error in average particle displacement is related to the Gaussian peak-finding algorithm and subpixel accuracy. With this algorithm, typical peak position errors are in the range 0.05 to 0.1 pixel (Forliti, Strykowski & Debatin 2000; Wernet 2000). Using the worst-case error of 0.1 pixel, the relative error in displacement is approximately 0.6% of full scale.

The precision error (P) was assessed statistically from $P = z_c s$ where z_c is the confidence coefficient and s is the standard deviation of the sample of I readings (or images). The latter is defined as follows:

$$s = \sqrt{\frac{1}{I-1} \sum_{k=1}^M (U_k - \bar{U})^2}, \quad (7)$$

where the mean velocity is defined by the equation:

$$\bar{U} = \frac{1}{I} \sum_{k=1}^M U_k. \quad (8)$$

The standard approach is to use the t -distribution in circumstances where the standard deviation s is itself an unknown quantity (Wernet 2000). Coleman & Steele (1995) recommend that, for $I \geq 10$, $z_c = 2$ for a 95% confidence interval. Since the sample size I is at least 30, $z_c = 2$ is adopted. In order to combine errors from the two sources, it is useful to express the precision uncertainty as a relative standard deviation, i.e. as $\hat{s} = s/\bar{U}$. The combined measurement uncertainty is then obtained from the square root of the sum of the squared uncertainties: $\sigma_U = \sqrt{B^2 + \hat{s}^2}$. Typical values of the relative standard deviation in the external-flow region and in the interfacial region are 2% and 3%, respectively. In the interior of the porous medium, time-averaged mean velocities are very low, particularly at higher values of ϕ , and so relative deviations are high. For example, the relative standard deviation is about 7.5% for $\phi \geq 0.04$ and 15% for higher values of ϕ .

3. Results and discussion

3.1. Preliminary results

This section reports on particular experimental issues. One issue was the number of samples or images (I) required to obtain a statistically converged mean velocity. To determine the number, velocity measurements were made in the annulus between the two concentric cylinders without the rods present. Mean velocities and standard errors were evaluated for sample sizes between 15 and 45. The results in figure 3(a) indicate that the mean velocity is independent of sample size for I in this range, and figure 3(b) demonstrates that the relative standard error is also nearly independent of I provided that I is greater than about 30. Therefore, in the tests which followed, 30 or more images were processed to obtain mean flow characteristics.

Another issue was accuracy of the mean velocity values, and this issue was addressed by comparing a measured velocity distribution with a known velocity profile. To this end, measurements were obtained in the annulus without the rods, and figure 4

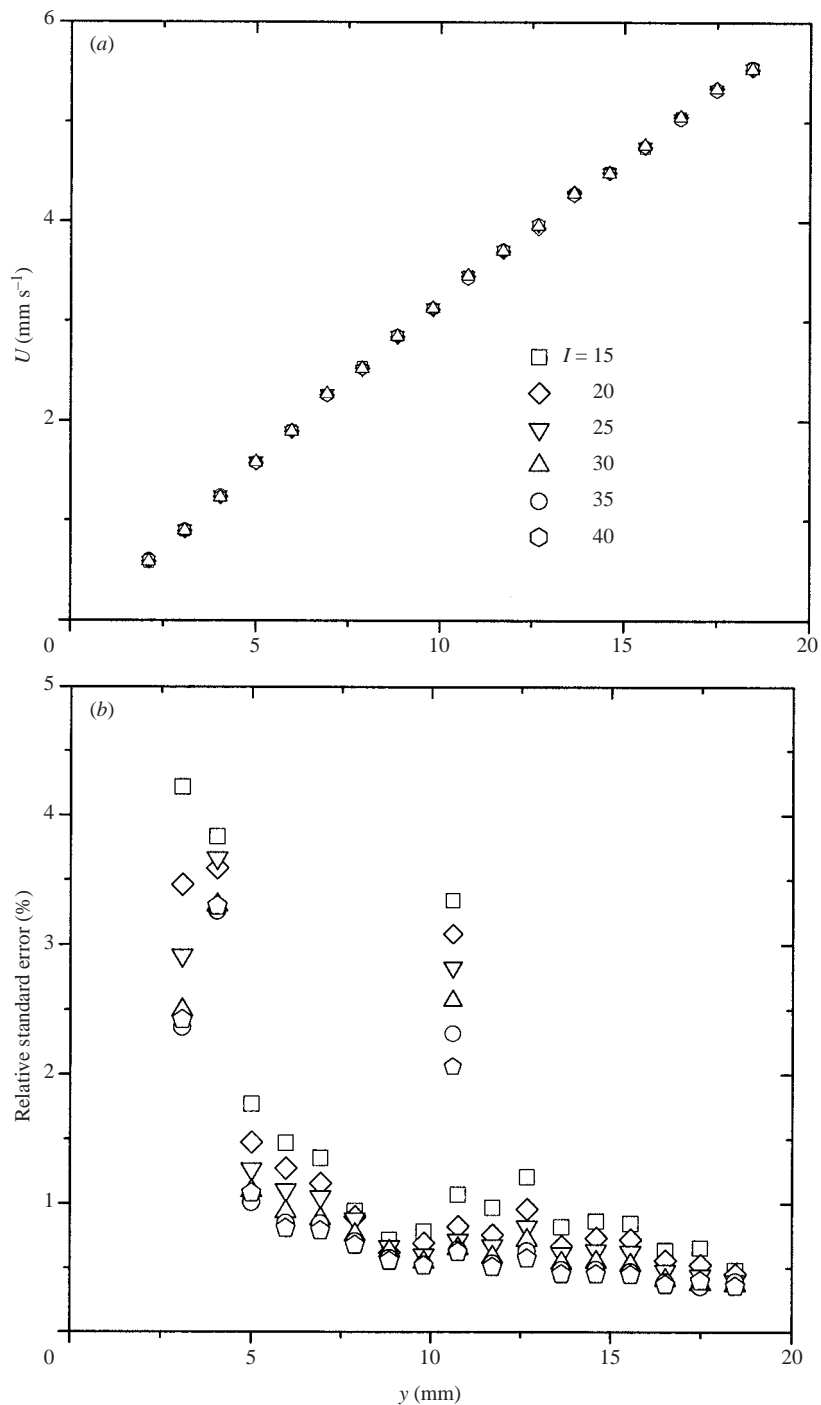


FIGURE 3. Preliminary velocity measurements in annulus without rods present to determine the minimum number of samples required to evaluate mean velocity. Sample sizes between 15 and 40 were explored. The mean velocity profiles are shown in (a) and distributions of the standard error normalized by the local mean velocity are shown in (b).

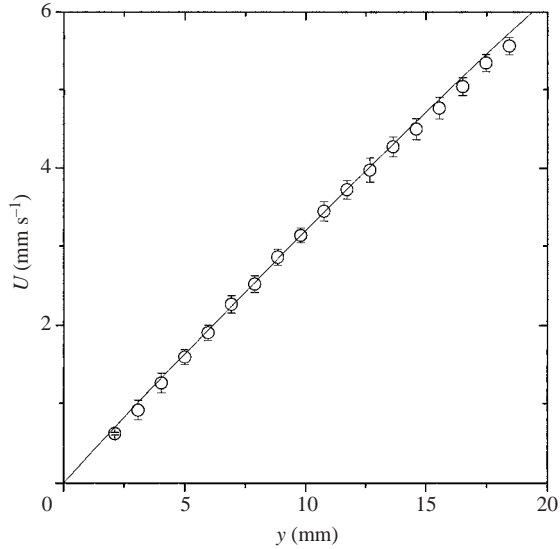


FIGURE 4. Comparison between \circ , measurement and —, exact solution for circular Couette flow in an empty space between a fixed inner cylinder and an outer rotating cylinder. The error bars represent one standard deviation.

presents the data along with the exact solution for circular Couette flow. The figure demonstrates good agreement except close to the outer cylinder where the data are slightly below solution values.

The final concern was the effect of inertia, and thus velocity measurements were obtained at Reynolds numbers well below unity so that the data should be independent of Reynolds number. In the present work, $Re = U_o d / \nu$, where d is the rod diameter, and Re was varied from 0.05 to 0.2. Typical results, obtained for $\phi = 0.052$ (circular rods) at $Re = 0.05$ and 0.14, are shown in figure 5. It is apparent that the two sets of data collapse within measurement uncertainties and therefore are independent of Reynolds number. Since Reynolds numbers for the test conditions in table 2 are within the same range, inertia should not be a factor in the results presented below.

3.2. Onset of circulation and its dependence on rod geometry

A side objective of our work was to investigate further the conditions under which secondary motion appears in the flow, that is, to determine the value of ϕ when eddies are first visible between the first two circles of rods, and to determine if this minimum value depends on rod shape. To this end, we examined maps of velocity vectors, and figures 6 to 8 show typical instantaneous velocity vectors for $0.025 \leq \phi \leq 10$ for circular, square and triangular rods. Figure 6 (for circular rods) reveals no secondary motion for $\phi = 0.025$ and 0.04, although the velocity fields are significantly altered by the rods. Eddies are evident, however, for $\phi = 0.052$ and 0.10, and were found at $\phi = 0.16$ as well (not shown). The present results for ϕ of 0.052 and 0.10 are qualitatively similar to those from the numerical calculations of Larson & Higdon (1987) for $\phi = 0.10$. Experimentally and theoretically, the centres of the eddies are very close to the outermost rods. Larson & Higdon (1987) reported circulation for $\phi = 0.042$, with the eddy centre close to the second row, but our measurements do not reveal any secondary motion for $\phi = 0.04$. Larson & Higdon also found circulation

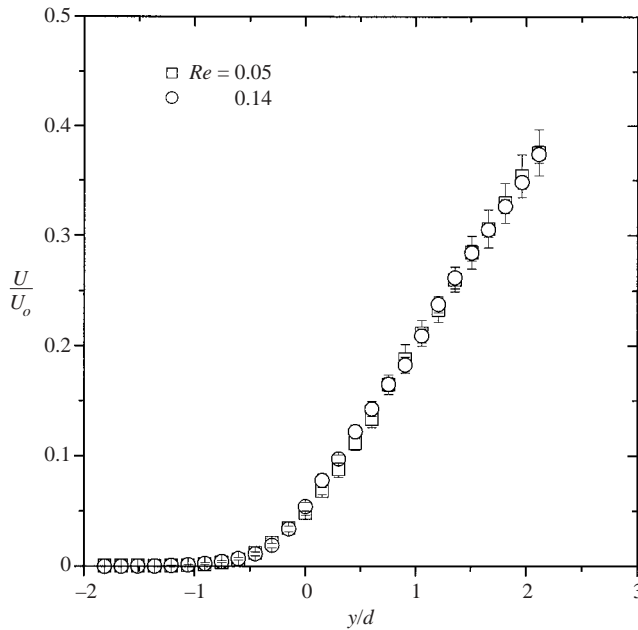


FIGURE 5. Preliminary measurements to explore inertia effect. The velocity profiles pertain to full array of circular rods at $\phi = 0.052$. The Reynolds number (Re) is based on the speed of the outer rotating cylinder (U_o) and diameter of the rod (d). The velocity is normalized by U_o and distances are made dimensionless by d . The error bars represent one standard deviation.

for $\phi = 0.03$, but the centre was below the second row, a region which could not be explored in the present work. In the PIV measurements reported by Shams *et al.* (2003), secondary motion was observed between the first two circles of rods for $\phi = 0.052$ and 0.10, but not for $\phi = 0.025$. Hence, those results and the present ones are consistent. Whereas the earlier results indicate that circulation starts when ϕ is between 0.025 and 0.052 for a square array of rods, the present results narrow the range to between 0.04 and 0.052.

As for secondary motion with other rod shapes, the velocity vectors for square rods (figure 7) show circulation for ϕ values of 0.04 and above, while similar plots for triangular rods (figure 8) show secondary motion only for $\phi = 0.10$ and 0.16 (not shown). The centres of circulation for both rod shapes are located close to the interfacial rods, similar to the finding with circular rods. Therefore, figures 6 to 8 clearly demonstrate that the onset of circulation between the first two circles of rods depends on the shape of the rods.

3.3. Identification of the interface

When an analytical solution is found to an equation governing the flow field, it is generally necessary to specify conditions at the boundaries. Since the present work is concerned with the ‘slip velocity’, the velocity at the interface between the outer channel and the porous medium, the interface must be clearly defined because the velocity in that region changes rapidly in the transverse direction. In previous studies, the interface has varied somewhat. Larson & Higdon (1987), for example, chose the interface to be the plane passing through the axes of the interfacial row of rods. Other workers, such as J&D and Beavers & Joseph (1967), selected the surface tangent to the outermost edge of the medium. Sahraoui & Kaviany (1991) chose the same nominal

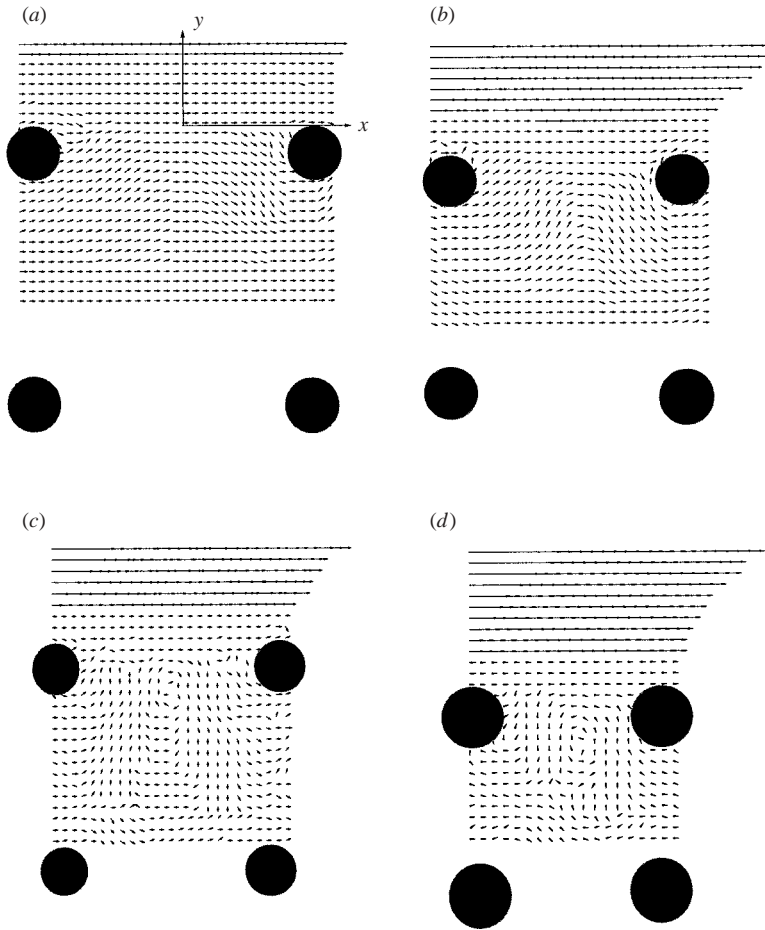


FIGURE 6. Instantaneous velocity vectors to show presence or absence of secondary motion in full array of circular rods at (a) $\phi = 0.025$; (b) 0.04; (c) 0.052; (d) 0.1. The solid circles represent four adjacent rods in a unit cell.

interface, $y = 0$, but analysed the sensitivity of the dimensionless slip coefficient α to interface location and showed that α depends critically on location. Even at a small distance above the nominal surface, for example at $y = 0.05d$ where d is the rod diameter, α is 50% lower than the true value (i.e. $U_s/\sqrt{k}\dot{\gamma}$ is 50% higher). Their findings dictate that the interface in our experiment must be located accurately.

Like most of the prior studies, the interface in this study is defined as the circle or cylindrical surface which is tangent to the outer edges of the outermost rods. This choice is the most realistic one for flow calculations because it represents the first contact of the outer flow with the array of rods, i.e. with the porous medium. Locating the interface precisely presents a challenge to the experimentalist, especially when using PIV, because particle data are averaged over a finite region to obtain a local velocity. Furthermore, it is not always possible to locate the centre of the interrogation region on the interface itself. These aspects add uncertainty in determining the average velocity along the interface, i.e. in determining the slip velocity. In the present work, it was possible to obtain the interface to within ± 0.3 mm or half of the side dimension of an interrogation region. Since the velocity changes rapidly in the interfacial region,

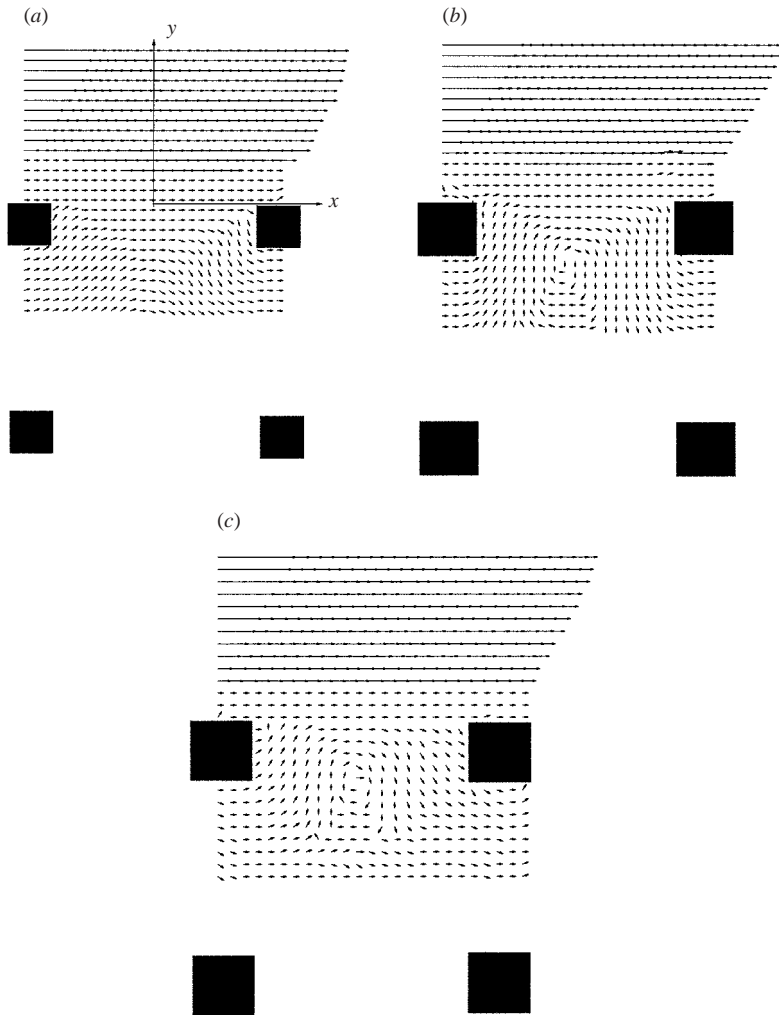


FIGURE 7. Instantaneous velocity vectors to show presence or absence of secondary motion in full array of square rods at (a) $\phi = 0.025$; (b) 0.04; (c) 0.05. The solid squares represent four adjacent rods in a unit cell.

a sensitivity analysis was carried out to estimate the variation in mean velocity in the interfacial region. In this analysis, a linear velocity distribution was assumed in the interfacial region and velocities were estimated by interpolation. It was found that the mean velocity could vary by as much as 10% within ± 0.3 mm of the interface.

Within a unit cell, the true interface is an arc. However, because the radius of curvature is large, the interface was taken to be the straight line connecting the tops of adjacent rods. This approximation creates an error, which was analysed by assuming a linear velocity distribution, as was done before. The error is a maximum at the high point of the arc and increases as the solid volume fraction decreases. The velocity there was found to be no more than 1.5% higher than the value on the straight line, for $\phi = 0.01$ and 0.025. This is the maximum error because the error decreases as ϕ increases and the arclength decreases.

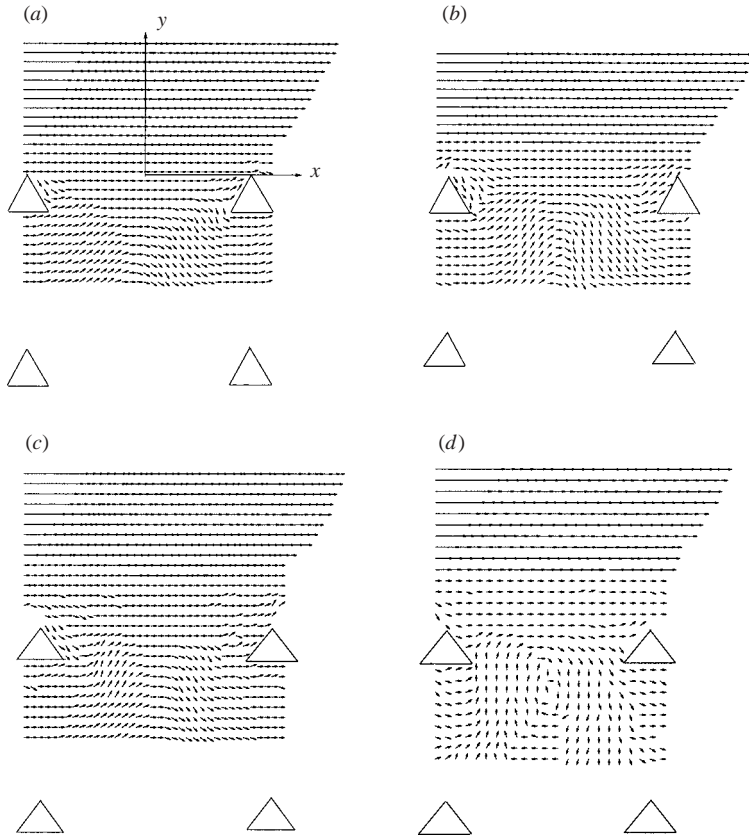


FIGURE 8. Instantaneous velocity vectors to show presence or absence of secondary motion in full array of triangular rods at (a) $\phi = 0.025$; (b) 0.04; (c) 0.05; (d) 0.10. The open triangles represent four adjacent rods in a unit cell.

3.4. Effects of interior rods and solid volume fraction on the mean flow

We now focus on the method of calculating the mean velocity, preliminary to finding the effects of solid volume fraction and of interior rods on the mean flow. For the two-dimensional flow field created by the experiment, the spatially averaged velocity $\langle U(y) \rangle$ is defined as:

$$\langle U(y) \rangle = \frac{1}{L} \int_{-L/2}^{L/2} U(x, y) dx. \quad (9)$$

where $U(x, y)$ is the local mean velocity obtained in a particular interrogation region using a minimum of 30 images. The streamwise coordinate x is measured from the plane midway between rods so that $\langle U(y) \rangle$ is evaluated over the interval between adjacent rods at a constant value of y .

We first present distributions of the local mean velocity $U(x, y)$ for two test conditions, one with and one without circulation. The goal is to illustrate the velocity field inside the porous medium because this type of micro-scale information is not available in the literature. This information, along with the velocity vectors in figures 6 to 8, will be useful in understanding and predicting convective heat and mass transfer rates in a fibrous porous medium. Figure 9 shows velocity distributions in the

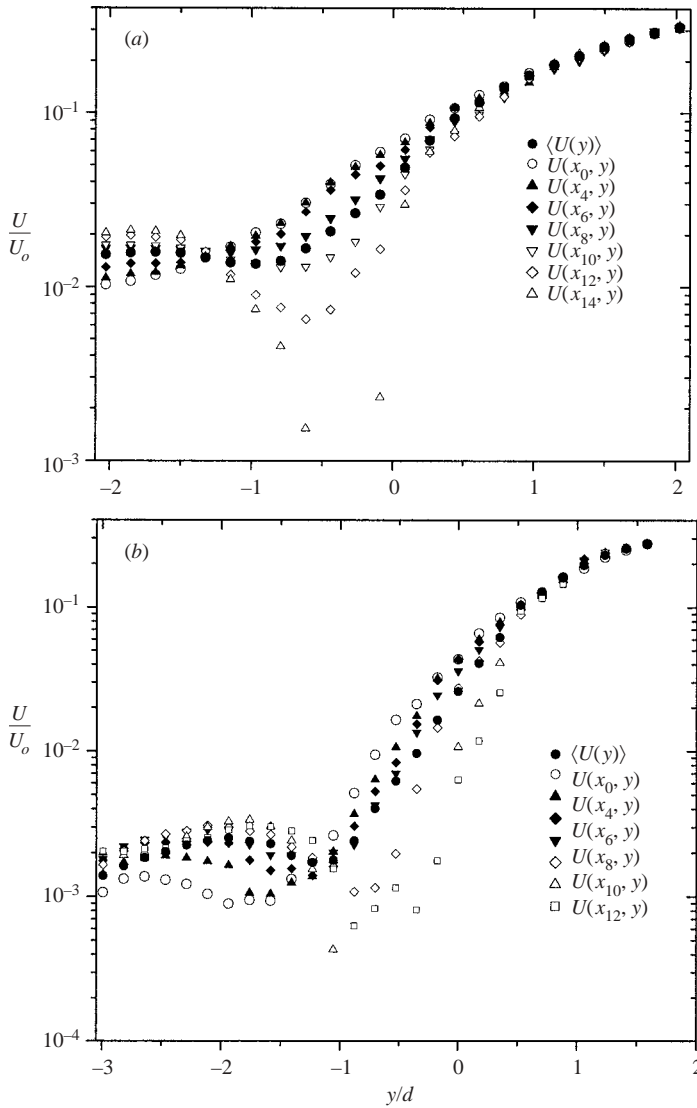


FIGURE 9. Distribution of spatially averaged velocity profiles $\langle U(y) \rangle$ and profiles obtained at various x -planes between the mid-plane (x_0) and adjacent right-hand rods. The results pertain to full array of circular rods at (a) $\phi = 0.025$ which reveal no secondary motion, and (b) $\phi = 0.052$ where secondary motion was observed. The velocity is normalized by U_o and distances are made dimensionless by diameter of the rod d .

interfacial region of circular-rod arrays for $\phi = 0.025$ and 0.052 . Because the velocity distributions are nearly symmetrical about the mid-plane ($x = 0$), only data in one half plane (the right-hand one) are shown. A logarithmic scale is necessary for the velocity because of its large range in values. In the external flow, i.e. for $y/d > 0.5$, the velocity profiles are nearly independent of x , as expected. However, significant differences are observed at the interfaces and within the arrays. In the region $-1 < y/d < 0.5$, for example, both plots of figure 9 show that velocities at the mid-plane, $U(x_0, y)$, are higher than those closer to the rods. There are also specific differences between the velocity profiles for $\phi = 0.025$ and 0.052 inside the porous medium. For example,

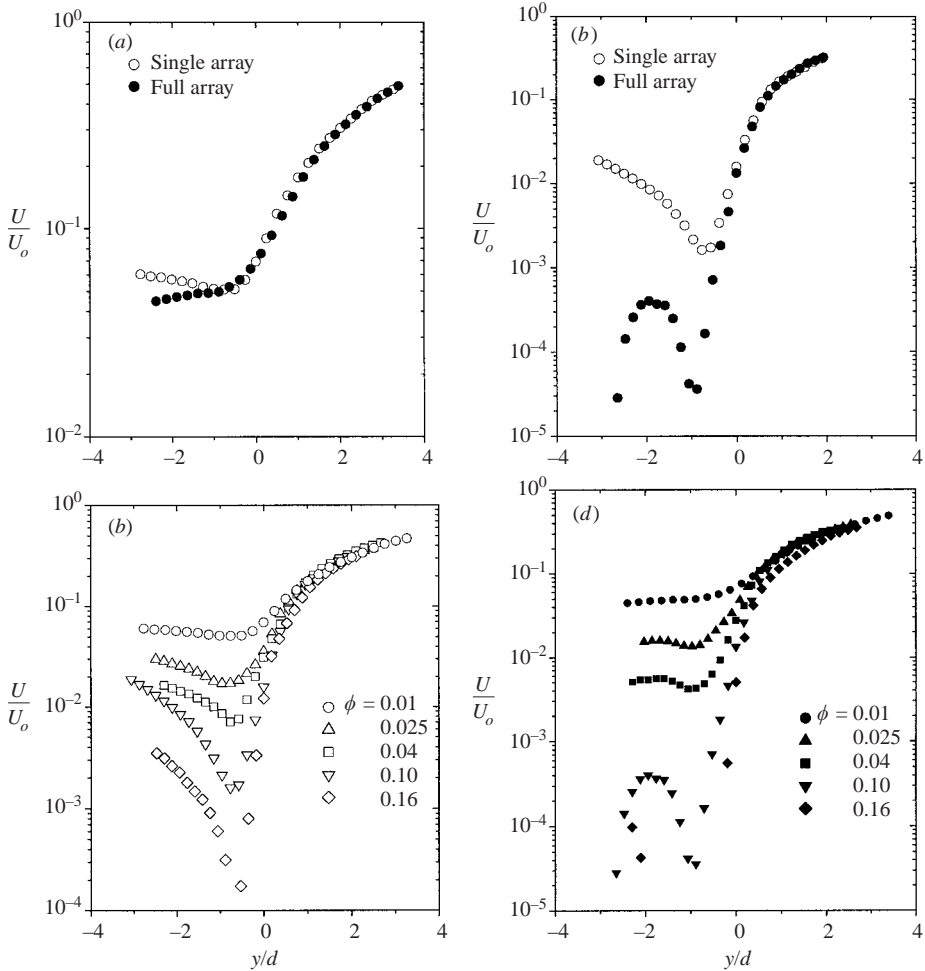


FIGURE 10. Distributions of mean velocity profiles to demonstrate the influence of interior rods and solid volume fraction ϕ in circular array of rods. (a) and (b) compare single versus full arrays of rods at $\phi = 0.01$ and $\phi = 0.10$, respectively; (c) and (d) compare velocity profiles at various solid volume fractions for single and full arrays, respectively.

the mean velocity profile naturally decays more rapidly for the higher solid volume fraction, $\phi = 0.052$. Furthermore, the mid-plane velocity decays monotonically for $\phi = 0.025$, while for $\phi = 0.052$ the mid-plane profile has a minimum at the circulation centre, followed by a gradual increase and then a decrease as the second circle of rods is approached. The spatially averaged velocity for $\phi = 0.025$ is also different from that for $\phi = 0.052$ inside the rods. That is, $\langle U(y) \rangle$ for $\phi = 0.025$ is nearly constant for y below about $-d$, while in the same region, for $\phi = 0.052$, $\langle U(y) \rangle$ increases with depth from a minimum value at $y/d \approx -1$ to a maximum value, and then it declines. Some of these differences are due to secondary motion. That is, circulation was observed for $\phi = 0.052$, but not for $\phi = 0.025$. In general, the data in figure 9 are consistent with the instantaneous velocity vectors shown in figure 6.

To demonstrate the influence of interior rods, the profiles $\langle U(y) \rangle$ for single and full arrays of circular rods are compared in figures 10(a) and 10(b), for $\phi = 0.01$ and $\phi = 0.1$, respectively. Figure 10(a) shows that the profiles for the two arrays

collapse reasonably well in the outer flow and in the interfacial region. The only significant difference is observed in the region $y/d < -1$, where the velocity for the full array is typically 10% lower than that for the single circle. Figure 10(b) reveals the same collapse in the outer and interfacial regions for $\phi = 0.10$. Below the interface, however, strong differences are observed, both in shape and magnitude. The difference in shape is partly due to the secondary motion within the full array. Apart from shape, velocities inside the full array are several orders of magnitude below those for the single array.

The effects of solid volume fraction on single versus full arrays are shown in figures 10(c) and 10(d). These figures demonstrate that the velocity decays much more rapidly as the solid volume fraction increases. That is, with more rods, the flow penetrates the porous medium less, as we expect. The figures also show that, although velocities are very small below the first circle for both arrays, they are generally several-fold higher behind the single circle. Corresponding data obtained with square and triangular rods demonstrate similar trends and therefore are not shown.

3.5. Determination of the slip velocity

The quantity of most interest in the interfacial region is the slip velocity. In this work, the slip velocity U_s is evaluated from:

$$U_s = \frac{1}{L} \int_{-L/2}^{L/2} U(x, 0) dx, \quad (10)$$

which is the integral along the straight line taken to be the interface. The location of this line, while easily drawn on paper, is difficult to determine experimentally. To demonstrate the variation of mean velocity with interface location, plots of $U(x, y)$ at different y values in the interfacial region are shown in figure 11(a) for a typical case. Data are presented for three adjacent strips of interrogation planes: at the nominal interface y_0 ; at the plane immediately below y_{-1} ; and at the plane just above y_{+1} . The width of the interrogation area for this particular test is 0.6 mm. The rapid variation of the mean velocity from one plane to the next, as shown in the figure, required exceptional carefulness in determining the interface. To identify the interface, digitized images – containing the outermost pair of rods – were overlaid onto the velocity vectors. Then, by carefully inspecting the velocity vectors and the edges of the outermost rods, the interface was determined. In a few cases, the interface was located between adjacent strips of interrogation planes so that the slip velocity was evaluated as the average value determined from the two adjacent planes. The maximum error in determining the slip velocity was estimated to be 10%.

Figure 11(b) shows typical distributions of $U(x, 0)$ for circular and triangular rods scaled by the maximum velocity and by the distance L between the rods. In all cases, non-zero velocities were obtained in interrogation regions occupied by the rod, for example, at $x/L = \pm 0.5$, where U should vanish. The contribution of these non-zero values to the slip velocity was estimated to be less than 0.5%.

To obtain the slip velocity, the integral in (10) was found in two ways: by direct graphical integration of the experimental data; and by fitting curves to the experimental data and graphically integrating the curves. Typical curve fits are shown in figure 11(b), and are seen to represent the data reasonably well. In fitting them to the data, the curves were forced to have zero values of U at $x/L = \pm 0.5$ in order for the curves to be realistic. The values of U_s obtained by the two methods were found

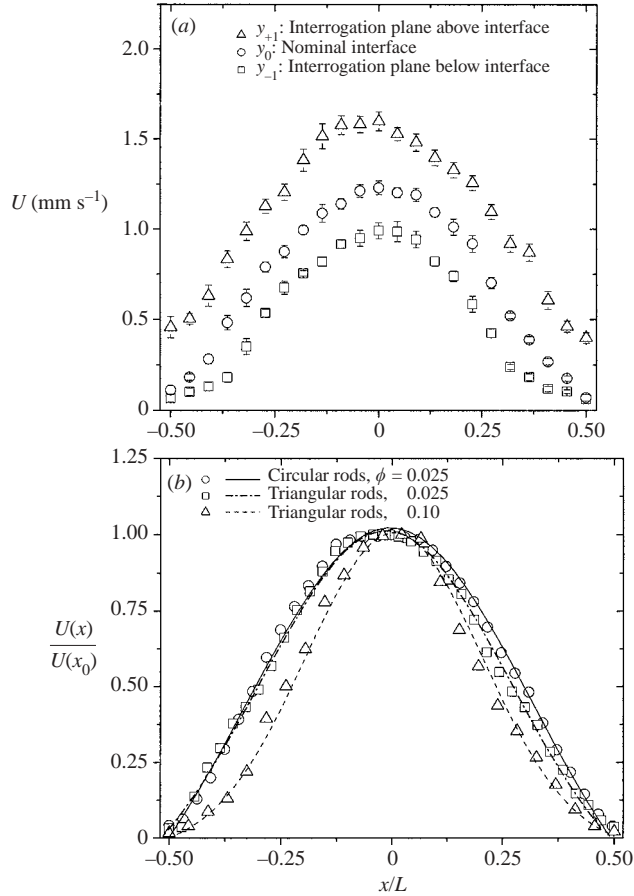


FIGURE 11. Velocity distributions at the interface of porous medium and plain medium. (a) Shows velocity profiles at three adjacent strips of interrogation planes to demonstrate rapid variation of velocity in the interfacial region, and (b) shows typical velocity distributions at the interface of full arrays of circular and triangular rods. The gap between the outermost circle of rods and the outer rotating cylinder is approximately 24 mm. The lines are curve fits to experimental data.

to agree within measurement uncertainties. For consistency, the values of U_s to be presented shortly were obtained by the curve fitting technique.

3.6. Dimensionless slip velocity

3.6.1. Normalization by the speed of the outer cylinder

It is useful to present values of the slip velocity in dimensionless form, especially for design purposes. For the simple shear flow investigated here, the obvious velocity scale is the speed of the outer cylinder, U_o , and hence values of U_s/U_o are presented in the two plots of figure 12. Data for single and full arrays of circular and square rods are compared in figure 12(a). The error bars represent measurement uncertainty at 95% confidence level. The figure reveals that the dimensionless slip velocity is almost independent of the number of circles of rods in the array. That is to say, the interior rods do not significantly influence the flow field at the interface. Furthermore, slip velocities for the square and circular rods differ by only a small amount.

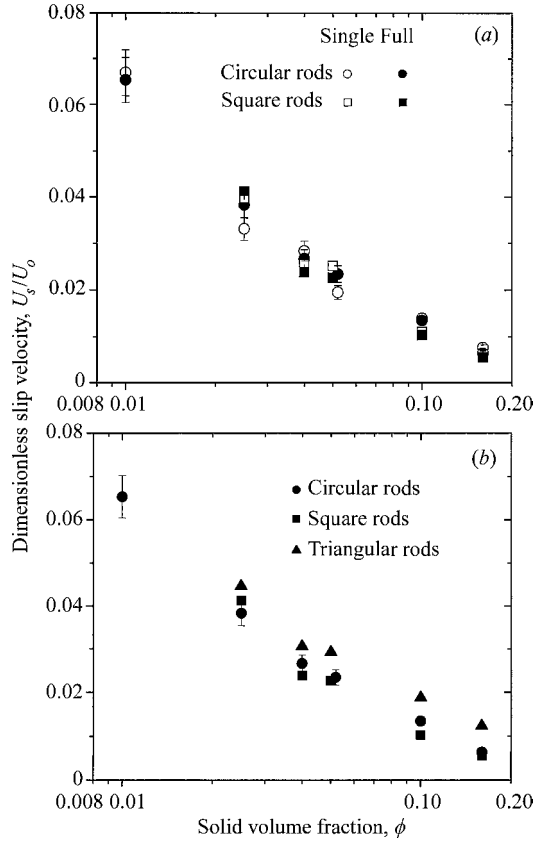


FIGURE 12. Distribution of slip velocity U_s normalized by the wall velocity U_o : (a) shows U_s/U_o for single versus full arrays of circular and square rods. (b) compares U_s/U_o for full arrays of circular, square and triangular rods. The error bars represent measurement uncertainty.

Dimensionless slip velocities for full arrays of the three different rod shapes are given in figure 12(b). The three data sets are qualitatively similar and, to a first approximation, the slip velocity is independent of rod shape. The highest slip velocity occurs with the triangular rods. Both plots of figure 12 show how the slip velocity decreases with solid volume fraction. For the present range of solid volume fractions, from 0.01 to 0.16, there is close to a decade of drop in the slip velocity. That is, the slip velocities for $\phi = 0.01$ and $\phi = 0.16$ are, respectively, 7% and 0.7% of the speed of the outer cylinder. The plots show that the dimensionless slip velocity for $\phi \geq 0.10$ is less than 2%, so that the no-slip boundary condition may be a reasonable approximation at the interface for $\phi \geq 0.10$. With such small velocities, there appears to be little point in finding slip velocities for ϕ above 0.2.

3.6.2. Normalization by the shear rate and permeability

Following the work of J&D, the slip velocity U_s is also expressed in the dimensionless form $U_s/\sqrt{k} \dot{\gamma}$, where k is the permeability and $\dot{\gamma}$ is the shear rate evaluated at the interface; i.e. $\dot{\gamma} = \partial U/\partial y|_{y=0+}$. The dimensionless group $U_s/\sqrt{k} \dot{\gamma}$ is more useful than U_s/U_o because it depends on local conditions and not on less relevant far-field conditions. This dimensionless slip velocity is equivalent to the inverse of the dimensional slip coefficient α proposed by Beavers & Joseph. Using the

	ϕ	U_o (mm s ⁻¹)	U_s (mm s ⁻¹)	$k^{1/2}$ (mm)	γ (s ⁻¹)	$U_s/\gamma k^{1/2}$	U_s/U_o (%)
(a)	0.01	20.82	1.394	9.98	0.457	0.306	6.69
	0.025	24.91	0.823	5.35	0.521	0.295	3.31
	0.04	21.46	0.607	3.79	0.581	0.276	2.83
	0.052	20.82	0.406	3.10	0.471	0.278	1.95
	0.10	24.91	0.347	1.80	0.722	0.267	1.39
	0.16	22.52	0.171	1.16	0.563	0.262	0.76
(b)	0.01	20.12	1.314	9.98	0.434	0.303	6.53
	0.025	21.33	0.816	5.35	0.565	0.270	3.83
	0.04	23.04	0.613	3.79	0.634	0.255	2.66
	0.052	25.14	0.608	3.10	0.804	0.242	2.34
	0.10	19.36	0.261	1.80	0.614	0.236	1.35
	0.16	20.33	0.129	1.16	0.474	0.235	0.64

TABLE 3. Summary of test parameters for (a) single and (b) full arrays of circular rods; U_o is the speed of (outer) rotating cylinder, U_s is the slip velocity, k is permeability, γ is the shear rate at the interface.

group $U_s/\sqrt{k} \dot{\gamma}$ will facilitate comparisons between the present data and prior results, including results presented in terms of α .

Using this dimensionless group requires evaluation of the velocity gradient, but estimating the derivative directly from velocity data is prone to error because of scatter in the data. Therefore, we used a least-squares curve fit to experimental data to obtain an accurate estimate of the shear rate. High-order polynomials, typically with 5 to 9 terms, with y -steps of 0.1 mm were used. Accuracy of fit was assessed by evaluating the coefficient of determination, R^2 , and the value of this quantity for each curve was higher than 0.99. The shear rates were obtained by differentiating these curves and the results smoothed over five data points. These five locations cover a distance of 0.5 mm, which is comparable to the dimension of an interrogation region. As for the permeability k , it was determined from (1) for the arrays of circular rods. The values of $\dot{\gamma}$ and k used for the calculations are included in table 3.

Values of the dimensionless slip velocity $U_s/\sqrt{k} \dot{\gamma}$ are presented in figure 13. The error bars in this figure represent measurement uncertainty at 95% confidence level. This plot is the single most important one in the paper for it compares theory with experiment and single versus full arrays, over a wide range in solid volume fraction. Figure 13 demonstrates that the dimensionless slip velocity for the single row of rods is no more than 10% higher than the corresponding value for a full array. The figure also shows that $U_s/\sqrt{k} \dot{\gamma}$ is nearly constant, because it decreases from about 0.3 at $\phi = 0.01$ to about 0.24 at $\phi = 0.16$. This drop in $U_s/\sqrt{k} \dot{\gamma}$ is small compared with the decade drop in figure 12(b), where U_o was used as the characteristic velocity.

3.7. Comparisons with prior work

In this section, we compare the present results with prior experimental and numerical results and also with values predicted from the Brinkman model. Theoretical values of $U_s/\sqrt{k} \dot{\gamma}$ from J&D are part of figure 13. As described in §1, the results in J&D were obtained for planar Couette flow. However, those results can be compared with the present ones because the radius of curvature in our experiment is large enough that curvature can be ignored. As figure 13 shows, the present experimental data

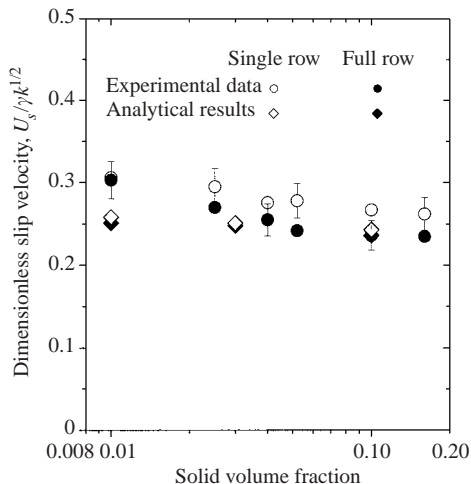


FIGURE 13. Distribution of dimensionless slip velocity $U_s / \sqrt{k} \dot{\gamma}$ for circular rods. The figure compares present experimental data with previous theoretical values (J&D). The error bars represent measurement uncertainty.

and the analytical results are in reasonable agreement, the maximum deviation being about 10%.

The data shown in figure 13 also show that the dimensionless slip velocity is only 24–30% of the value of unity implied by the Brinkman equation. That is, the Brinkman equation predicts significantly greater penetration of the outer flow than that measured in the present experiment. Such a discrepancy is not surprising when it is remembered that the Brinkman equation describes the velocity averaged over several pore sizes; as such, the bulk velocity should not be expected to be accurate in the interfacial region which, as shown here, is only a fraction of the pore size.

In the experiments of Beavers & Joseph, natural and manufactured porous media were studied in pressure-driven flows. They did not report the solid volume fractions for their materials and so the values given later by Kim & Russel (1985) are used. When their results, which are presented in terms of the slip coefficient, are converted to the dimensionless slip velocity, the values of $U_s / \sqrt{k} \dot{\gamma}$ for $\phi \approx 0.2$ range from 0.25 to 1.3, depending on the pore size of the material. These values are in keeping with present values, even though the geometries of the porous media are very different.

As reported in §1, Taylor (1971) measured the slip velocity at the interface of a model porous medium and Richardson (1971) predicted velocity values from a solution of the Stokes equation. Their model was a series of deep rectangular grooves in a plate, and for this geometry they found that the slip coefficient depends on s/t , the ratio of groove width to wall thickness. At a solid volume fraction ϕ of 0.2 (i.e. $s/t = 0.2$), they obtained a value of 0.5 for $U_s / \sqrt{k} \dot{\gamma}$. This value is almost twice as high as the value obtained at $\phi = 0.16$ in the present work, which is not surprising because the grooves are aligned with the flow and thus offer less resistance to penetration. Their results also show a maximum value of 0.7 for $U_s / \sqrt{k} \dot{\gamma}$, in the limit of zero solid volume fraction.

Sahraoui & Kaviany (1991) used a numerical technique to determine the slip coefficient for a periodic structure of rods in Poiseuille flow. In terms of our notation, they found that $U_s / \sqrt{k} \dot{\gamma}$ is about 0.25 at $\phi = 0.2$, increasing to about 1.0 at $\phi = 0.5$. Their value at $\phi = 0.2$ is approximately equal to our value of 0.23 at $\phi = 0.16$.

However, our results suggest a weak decay of $U_s/\sqrt{k}\dot{\gamma}$ with ϕ , while their results indicate a rapid increase in $U_s/\sqrt{k}\dot{\gamma}$ with ϕ .

4. Conclusions

In the first part of the research programme, secondary motion was examined and its dependence on solid volume fraction and rod shape was investigated. Consistent with prior studies, the motion appeared for sufficiently high volume fractions. For circular rods, the minimum value of ϕ was found to be 0.052; for square and triangular rods, the minimum values were 0.04 and 0.10, respectively. While this circulation depends strongly on rod shape, geometry was found to have almost no influence on the characteristics of the mean flow in the interfacial region. That is, for a given solid volume fraction, the slip velocity normalized by the wall velocity was approximately the same for the three shapes of rod that were investigated. It was found that the interior rods significantly influence the flow in the interior, but not at the interface. More specifically, the slip velocity for a single row of rods was found to be almost identical to the velocity for a full array. This finding held over a wide range in solid volume fraction and for three widely different rod shapes.

For the range of solid volume fraction studied, $0.01 \leq \phi \leq 0.16$, the slip velocity and the parameter \sqrt{k} dropped by about a decade. Because the shear rate at the interface is not sensitive to the solid volume fraction, the dimensionless group $U_s/\sqrt{k}\dot{\gamma}$ is only weakly dependent on the solid volume fraction. To be more precise, the value of $U_s/\sqrt{k}\dot{\gamma}$ drops from 0.30 to 0.24 as ϕ increases 16-fold. The predictions of $U_s/\sqrt{k}\dot{\gamma}$ by J&D are in good agreement with the measurements obtained in this work.

We gratefully acknowledge the support of this work by the Natural Sciences and Engineering Research Council of Canada, through a Postdoctoral Fellowship to M. F. T. and through Research Grants to D. F. J. and I. G. C.

REFERENCES

- BEAVERS, G. S. & JOSEPH, D. D. 1967 Boundary conditions at a naturally permeable wall. *J Fluid Mech.* **30**, 197–207.
- BRINKMAN, H. C. 1947 A calculation of the viscous force exerted by a flowing fluid on a dense swarm of particles. *Appl. Sci. Res. A* **1**, 27–34.
- COLEMAN, W. H. & STEELE, W. G. 1995 Engineering application of experimental uncertainty analysis. *AIAA J.* **33**, 1888–1896.
- DAVIS, A. M. J. & JAMES, D. F. 2003 The slip velocity at the edge of a porous medium. *Transport Porous Media* **53**, 175–196.
- FORLITI, D. J., STRYKOWSKI, P. J. & DEBATIN, K. 2000 Bias and precision errors of digital particle image velocimetry. *Exps. Fluids* **28**, 436–447.
- JACKSON, G. W. & JAMES, D. F. 1986 The permeability of fibrous porous media. *Can. J. Chem. Eng.* **64**, 364–374.
- JAMES, D. F. & DAVIS, A. M. J. 2001 Flow at the interface of a model fibrous medium. *J. Fluid Mech.* **426**, 47–72 (referred to herein as J&D).
- KIM, S. & RUSSEL, W. B. 1985 Modelling of porous media renormalization of the Stokes equations. *J. Fluid Mech.* **154**, 269–286.
- LARSON, R. E. & HIGDON, J. J. L. 1986 Microscopic flow near the surface of two-dimensional porous media. Part 1. Axial flow. *J. Fluid Mech.* **166**, 449–472.
- LARSON, R. E. & HIGDON, J. J. L. 1987 Microscopic flow near the surface of two-dimensional porous media. Part 2. Transverse flow. *J. Fluid Mech.* **178**, 119–136.
- RICHARDSON, S. 1971 A model for the boundary condition of a porous material. Part 2. *J. Fluid Mech.* **49**, 327–336.

- SAHRAOUI, M. & KAVIANY, M. 1991 Slip and no-slip boundary conditions at interface of porous, plain media. *ASME/JSME Thermal Engng. Proc.* **4**, 273–286.
- SHAMS, M. 2000 Study of flow at the interface of a porous medium using particle image velocimetry. PhD thesis, University of Toronto, Canada.
- SHAMS, M., JAMES, D. F. & CURRIE, I. G. 2003 The velocity field near the edge of a model porous medium. *Exps. Fluids* (in press).
- TAYLOR, G. I. 1971 A model for the boundary condition of a porous material. Part 1. *J. Fluid Mech.* **49**, 319–326.
- WERNET, M. P. 2000 Development of digital particle imaging velocimetry for use in turbomachinery. *Exps. Fluids* **28**, 97–115.